XLVI CILAMCE
VITÓRIA - ES - BRAZIL - 2025
XLVI IBERO-LATIN AMERICAN CONGRESS ON COMPUTATIONAL METHODS IN ENGENEERING

GPU-Accelerated Regularized LBM with Curved Boundaries: Confinement Effects on Cylinder Wake Dynamics

M. Sakthivel, B.Y. dos Anjos, G.T. Choaire, L.A. Hegele Jr.

Department of Petroleum Engineering, Santa Catarina State University (UDESC)
Balneario Camboriu, Santa Catarina 88336-275, Brazil
sakthi.me12@gmail.com

Abstract. We present the curved boundary condition for the moments-based regularized lattice Boltzmann (MRLBM) framework in two-dimensional (2D) coordinates. The solver is based on the Bhatnagar-Gross-Krook (BGK) collision model with D2Q9 lattice stencils and developed on the GPU-architecture using CUDA leveraging the inherent locality of the LBM. The accuracy and capability of the solver in handling curved geometries is validated for the canonical benchmark problem of flow past a cylinder inside a channel considering the wall effects. A moments-based curved boundary condition is formulated to handle complex geometries on a uniform Cartesian grid, and the numerical stability is significantly enhanced through a regularization procedure. A extrapolation-based approach is adopted for the curved boundary treatment. Results of the simulation for moderate Reynolds number range ($Re = 20 - 120$) and for different blockage ratio $\beta_s = D/H$ are presented. The solver is carefully verified/validated with the experimental and numerical studies exists in the for Re = 100. Global time-averaged lift and drag coefficients, surface pressure coefficients, and vortex dynamics are rigorously investigated.

Keywords: Lattice Boltzmann Method (LBM), Regularization, Curved boundary, GPU, Cylinder

1 Introduction

Over the past few decades, lattice Boltzmann method (LBM) evolved as a powerful numerical tool over the conventional Navier-Stokes-based methods for computational fluid dynamics (CFD) simulations. Because of its mesoscopic and local nature of the governing lattice Boltzmann equation (LBE) makes it easy to implement and parallelize especially in GPU architectures. However, many studies in the literature reported that LBM typically requires finer mesh and is prone to numerical instability for higher-Reynolds numbers. Several approaches are proposed in the literature to address these limitations includes: (1) the multiple-relaxation-time LBM (MRT-LBM)[1], and (2) the regularized LBM (RLBM)[2–4]. Each methods has its own advantages and disadvantages, we adopted the regularized LBM, as it retains the simplicity of the BGK model while introducing a pre-collision regularization step. This step filters out non-hydrodynamic modes from the non-equilibrium distribution function, thereby enhancing stability and accuracy at high Reynolds numbers without significantly increasing computational cost. Additionally, memory usage in the regularized lattice Boltzmann method (RLBM) can be reduced by adopting a moment-based representation, where macroscopic moments are stored instead of the full distribution functions [5]. This study focuses on development of curved boundary condition for the moments-based regularized LBM (MRLBM) framework and evaluates its accuracy in handling curved geometries, an aspect not yet explored in existing MRLBM literature.We adopt the extrapolation-based approach for several compelling reasons. First, it preserves the simplicity and efficiency of Cartesian meshes, avoiding the costly mesh generation required by body-fitted methods. Second, it maintains excellent parallelizability and scalability - critical advantages for GPU-paralleized large-scale simulations. Most importantly, when combined with appropriate extrapolation schemes, this method can achieve second-order accuracy while effectively minimizing stair-casing artifacts at curved boundaries. To validate the developed moments-based curved boundary condition, we choose the canonical benchmark problem of flow past a circular cylinder inside the channel in two-dimensional coordinates consider the wall effects. We investigate the results for the moderate Reynolds numbers, $Re = 20 - 120$ to isolate three-dimensional effects and the effect of wall on the flow dynamics is investigated for different blockage ratios, $\beta_s = D/H$ for the range of $0.1 - 0.5$, where D is the diameter of the cylinder and H is the height of the bounded domain. The key investigation parameters include, time-averaged drag coefficient and root-mean-square (r.m.s) lift coefficient fluctuations, Strouhal number (St) for vortex shedding frequencies.

2 Numerical Methodology

This study employs a moments-based regularized lattice Boltzmann method (LBM) framework to simulate flow past a circular cylinder. The numerical approach combines three key components: (1) a regularized moments-collision for enhanced stability and efficiency, (2) a curved boundary treatment for accurate geometry resolution, and (3) an optimized computational domain to minimize boundary effects.

2.1 Regularized LBM Framework

The discrete lattice Boltzmann equation (LBE) that governs the evolution of particle distribution function in the microscopic momentum space with a finite number of velocity links $\boldsymbol{c}_i$ and it is given by [6],

$$f_i(\boldsymbol{x}+\boldsymbol{c}_i\Delta t, t+\Delta t) = \hat{f}_i(\boldsymbol{x},t) - \frac{\Delta t}{\tau}[\hat{f}_i(\boldsymbol{x},t) - f_i^{eq}(\boldsymbol{x},t)] \tag{1}$$

where, i denotes the lattice direction which depends on the lattice type, for D2Q9 model $i = 0,1,2...,8$ and $\boldsymbol{c_i}$ is the lattice velocity in the i direction, $\tau = 1/\omega$ is the relaxation time which denotes the time taken by the particles to reach the equilibrium state and ω is the relaxation frequency. In the present LBM framework, we utilize the moments-based regularized lattice Boltzmann method (MRLBM) [5, 7, 8]. First, the populations are reconstructed from the post-collisional moments $(\rho, \rho u_\alpha, \rho m^{(2)}_{\alpha\beta})$ (Eq. 5) as follows:

$$\hat{f}_i = \rho w_i \left(1 + a_s^2 u_\alpha c_{i\alpha} + \frac{1}{2} a_s^4 m^{(2)}_{\alpha\beta} H^{(2)}_{\alpha\beta,i}\right) \tag{2}$$

where $m^{(2)}_{\alpha\beta}$ is the second-order moments, w_i is weighing factor and a_s is the scaling factor equal to $\sqrt{3}$. Additionally, ρ is the fluid density, u_α is the macroscopic velocity vector and $H^{(2)}_{\alpha\beta,i} = c_{i\alpha}c_{i\beta} - \delta_{\alpha\beta}/a_s^2$ is the second-order Hermite polynomial function. It should be noted that, here ($\hat{}$) represents the regularized populations which is different from the original populations. With the populations reconstructed at the each lattice site, now the streaming step is performed using the regularized populations with the D2Q9 velocity set as follows:

$$f_i(\boldsymbol{x}+\boldsymbol{c}_i\Delta t, t+\Delta t) = f_i^*(\boldsymbol{x},t). \tag{3}$$

Here f^* represents the reconstructed population using post-collisional moments as given given by Eq. (2). After the streaming step, the populations f_i are known at every fluid site and the moments now are computed as,

$$\{\rho, \rho u_\alpha, \rho m^{(2)}_{\alpha\beta}\} = \sum_i \{f_i, f_i c_{i\alpha}, f_i H^{(2)}_{\alpha\beta,i}\} \tag{4}$$

Followed by the collision step in the moment space where the collision is performed on the second-order moments using the BGK collision operator as follows,

$$\rho^* m^{*(2)}_{\alpha\beta} = (1-\omega)\rho m^{(2)}_{\alpha\beta} + \omega \rho u_\alpha u_\beta, \tag{5}$$

The relation between the relaxation time and the kinematic viscosity ν is obtained from the Chapman-Enskog expansion and is given by,

$$\nu = \frac{1}{a_s^2}\left(\frac{1}{\omega} - \frac{\Delta t}{2}\right) \tag{6}$$

2.2 Moments-based regularized planar boundary implementation

For the collision step in Eq. (5), pre-collisional moments $(\rho, \rho u_\alpha, \rho m^{(2)}_{\alpha\beta})$ must be known at all nodes, including boundaries. Boundary nodes lack outgoing populations (O_s) from solid regions, requiring special treatment. Following Hegele et al. [4], pre-collisional moments are constructed using only known incoming populations (I_s) via:

$$\sum_{i\in I_s} f_i H^{(2)}_{\alpha\beta,i} = \sum_{i\in I_s} \hat{f}_i H^{(2)}_{\alpha\beta,i}. \tag{7}$$

Specific implementations are as follows:

- *Solid Boundary (Dirichlet):* Velocity is prescribed (no-slip, no-penetration). Density (ρ) and second-order moments are solved using Eq. (7) with mass conservation:

$$\sum_{i\in I_s} f_i = \sum_{i\in O_s} \left[(1-\omega\Delta t)\hat{f}_i + \omega\Delta t f_i^{eq}\right]. \tag{8}$$

- *Inlet boundary (Dirichlet):* Velocity is fixed. Density and second-order moments are solved using Eq. (7) with weak mass conservation:

$$\sum_{i\in I_s} f_i = \sum_{i\in I_s} \hat{f}_i. \tag{9}$$

- *Outlet boundary (Neumann):* Zero-gradient conditions ($\partial\rho/\partial n = 0$, $\partial \boldsymbol{u}/\partial n = 0$) are applied by setting $\rho_b = \rho_{int}$ and $\boldsymbol{u}_b = \boldsymbol{u}_{int}$. Second-order moments are then obtained from Eq. (7).

2.3 Moments-based regularized curved boundary condition

In the present curved boundary treatment, a smoothed physical curved geometry is modeled as a "staircase" boundary nodes. The computational lattice sites inside the physical boundary are characterized into three categories as shown in Fig. 1b: (i) wall points (physical curved boundary) and (ii) solid nodes (inside the wall) and (iii) boundary nodes where curved boundary condition is applied. The basic idea of extrapolation approach is that apply extrapolated boundary values at the boundary nodes such that the physical boundary value at the wall points are satisfied. Any macroscopic variables ($M = \{\rho, p, u_\alpha, M_{\alpha\beta}....\}$) can be extrapolated using the following

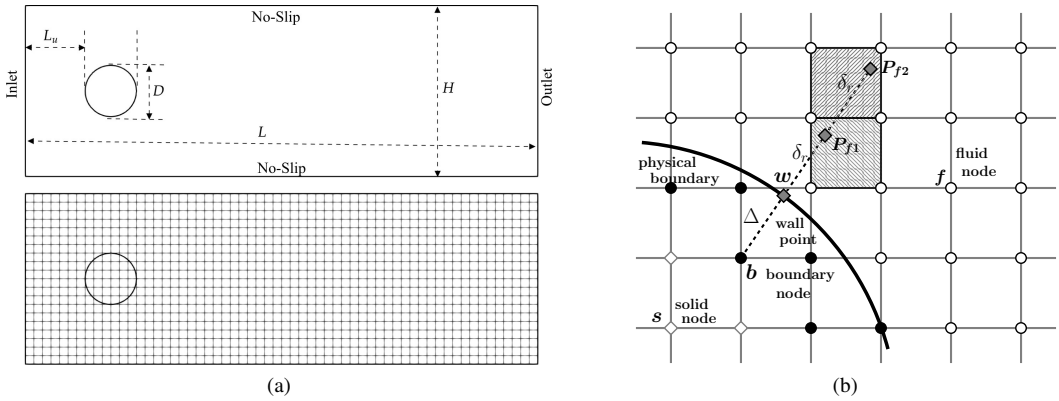


Figure 1. a) Computational domain and mesh. b) Curved boundary treatment: Layout for the three-point extrapolation approach. The schematic is not to scale and the actual domain is substantially larger to avoid boundary interference

expression [9]:

$$M^{(b)} = \frac{(2\delta_r^2 - \Delta^2 + 3\Delta\delta_r)}{2\delta_r^2} M^{(w)} + \frac{\Delta(\Delta - 2\delta_r)}{\delta_r^2} M^{(P_{f_1})} - \frac{\Delta(\Delta-\delta_r)}{2\delta_r^2} M^{(P_{f_2})} \tag{10}$$

where, b is the boundary point, w denotes the wall point (physical boundary) and P_{f_1}, P_{f_2} are the locations of two fluid points in the wall normal direction. The distance between the boundary node and the wall point is denoted by Δ and the distance between the reference points is denoted by δ_r. The wall values $M^{(w)}$ enforce Dirichlet conditions while $M^{(P_{f_i})}$ are obtained through bilinear interpolation from surrounding neighboring fluid nodes as shown in Fig. 1b. For no-slip boundaries (physical boundary), velocities at boundary nodes are computed via Eq. (10) with zero wall velocities. Density (ρ) and second-order moments (m_{xx}, m_{yy}, m_{xy}) are solved from the system obtained by mass conservation given by Eq. (8) and Eq. (7), respectively.

2.4 Hydrodynamic force calculation: Momentum exchange method

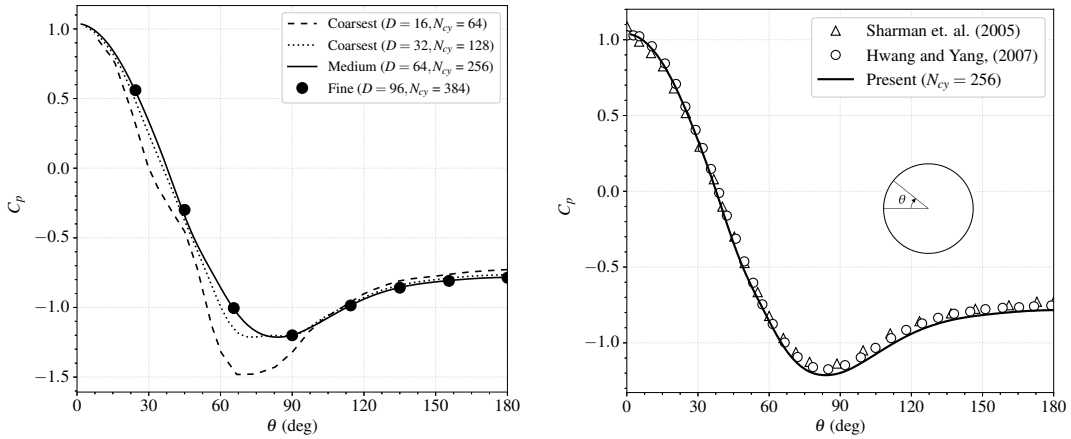
The hydrodynamic forces on immersed boundaries are computed using a momentum exchange approach and the force components (F_x, F_y) acting on the immersed boundary is obtained by:

$$F_\alpha = \sum_S \left(\sum_{i\in I_s} f_i(\boldsymbol{x}_b, t) c_{i\alpha} - \sum_{i\in O_s} f_i^*(\boldsymbol{x}_b, t) c_{i\alpha} \right), \tag{11}$$

where the inner summation represents the net momentum exchange between incoming populations f_i (post-propagation) and reconstructed outgoing populations f_i^* (post-collision) at each boundary node $\boldsymbol{x}_b$, while the outer summation integrates these contributions over all boundary nodes S that define the solid surface.

2.5 Computational setup and Numerical verification

Figure 1a shows the computational domain for flow past a cylinder in a two-dimensional Cartesian grid. To avoid boundary effects, the longer domain is considered of length $L = 60D$, with the cylinder positioned $15D$ from the inlet and $44D$ from the outlet. The baseline height is $H = 10D$. As illustrated in Fig. 2a, a grid convergence study using $D = 16, 32, 64$, and 96 lattice nodes showed less than 2% variation in key parameters (lift coefficient, pressure coefficient) between $D = 64$ and $D = 96$. Therefore, $D = 64$ was selected for all simulations, providing grid-converged solutions with computational efficiency. Two parameter studies were conducted: (1) Reynolds number effect: $H = 10D$ with varying Re. (2) Wall confinement effect: $Re = 100$ with $H = 2D, 4D, 5D, 8D, 10D$ ($\beta_s = D/H = 0.5, 0.25, 0.2, 0.125, 0.1$). The domain is bounded by solid top and bottom walls positioned at $H/2$



(a) (b)

Figure 2. a) Grid convergence study for flow past a cylinder at $Re = 100$. b) Numerical verification with literature data: Surface pressure coefficient (C_p) at $Re = 100$ (unbounded configuration).

from the cylinder center, as shown in Fig. 1b. No slip boundary conditions is applied on the immersed cylinder surface and top and bottom wall, and Neunmaan boundary condition is applied at the outlet boundary. An uniform constant inlet velocity u_o is imposed at the inlet boundary. The Reynolds number of the flow is defined as, $Re = u_o D/\nu$. The inlet velocity was fixed at $u_o = 0.1$ to maintain numerical stability. The specific τ values used to achieve the target Reynolds numbers were: $\tau = 1.46$, 0.844, 0.74, 0.692, 0.66, 0.628, and 0.607 corresponding to $Re = 20$, 50, 80, 100, 120, 150, and 180, respectively. The proposed moments-based boundary treatment demonstrates excellent agreement with literature data for $Re = 100$ cylinder flow with unbounded configuration (withou wall effects). As shown in Fig. 2b, the pressure coefficient (C_p) distribution matches closely with high-fidelity Navier–Stokes solutions from Sharman et al. [10] and Hwang et al. [11], particularly capturing the base suction coefficient and wake pressure recovery.

3 Results and Discussions

This section presents a comprehensive analysis of the flow dynamics around a circular cylinder, focusing on the effects of Reynolds number (Re) and blockage ratio (β_s). The key parameters investigated include: Surface pressure coefficient (C_p), Vortex dynamics, variation of vortex shedding frequency (St), time-averaged drag coefficient (C_D) and time-averaged root-mean-square (r.m.s.) lift coefficient ($C_{L,\mathrm{rms}}$). Time-averaged quantities were computed after the flow reached statistical stationary state, confirmed by monitoring the stabilization of root-mean-square values of the lift coefficient. The time-averaging of all the quantities was performed over 15 complete vortex shedding cycles, this corresponds to approximately 57,345 time steps. The vortex shedding frequency was determined from the oscillating lift coefficient signal $C_l(t)$. The time period between successive peaks (T_p) in the lift coefficient, and the shedding frequency was calculated as $f_s = 1/T_p$.

3.1 Surface pressure coefficient and the pressure recovery

The pressure coefficient (C_p) is a dimensionless parameter to describe the pressure distribution on a cylinder surface relative to the free-stream flow conditions and is computed as: $C_P = (p_w - p_\infty)/\frac{1}{2}\rho_\infty u_o^2$, where $p_w = \rho_w/a_s^2$ is the time-averaged pressure on the cylinder surface (wall points) and ρ_w is the density on the cylinder surface, and $p_\infty = \rho_\infty/a_s^2$ is the free-stream pressure. The time-averaged pressure coefficient distribution around a circular

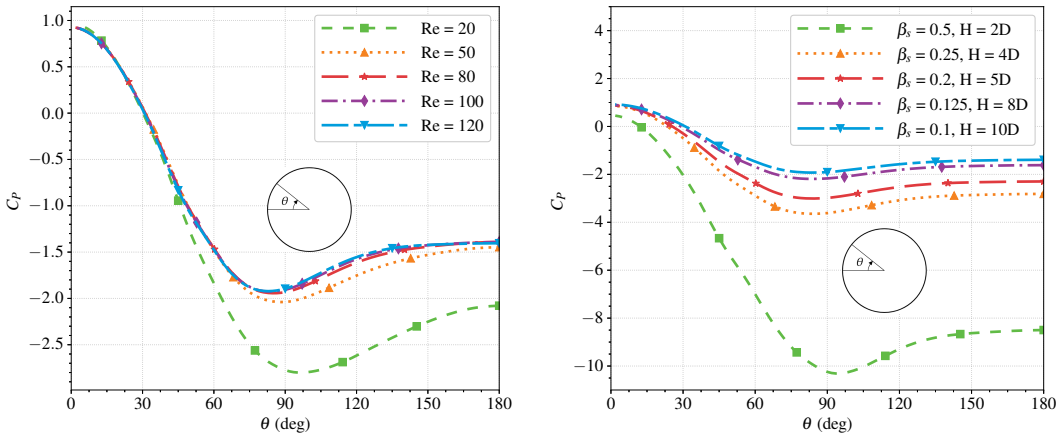


Figure 3. Comparison of surface pressure coefficient (C_p): a) for different Reynolds numbers at a fixed blockage ratio $\beta_s = 0.1$. b) for different blockage ratio (β_s) at a fixed $Re = 100$

cylinder is examined for Reynolds numbers (Re) ranging from 20 to 120 at a fixed $\beta_s = 0.1$ (Fig. 3a), as well as for varying blockage ratios (β_s) at a fixed $Re = 100$ (Fig. 3b). Due to symmetry about $\theta = 180°$, only the upper half ($0° \leq \theta \leq 180°$) is presented. The results reveal that the pressure decreases gradually along the cylinder surface up to the separation point, beyond which it increases due to the adverse pressure gradient in the wake region. The presence of the wall suppresses vortex shedding behind the cylinder, leading to minimal variations in pressure with increasing Re. However, the location of minimum C_p shifts upstream with higher Re, indicating earlier flow separation due to stronger inertial effects. In contrast, increasing the blockage ratio (β_s) which constricts the flow area causes the minimum C_p to shift downstream. This occurs because the accelerated flow delays separation, enhancing the adverse pressure gradient behind the cylinder. Consequently, the wake pressure drops more sharply at higher β_s.

3.2 Vortex dynamics and Shedding frequency (Strouhal Number)

As previously discussed, adverse pressure gradients on the rear half of the cylinder induce boundary layer separation, forming shear layers that roll into vortices above and below the cylinder, creating the wake. Fig. 4 shows normalized stream-wise vorticity contours for different Re and different β_s. For subcritical Reynolds numbers ($Re < 50$), the flow exhibits steady, symmetric vortices characteristic of creeping flow. As Re approaches the critical range (47-50), perturbations initiate the transition to periodic vortex shedding. In the moderate Re regime ($50 \leq Re \leq 120$), vortex dynamics show increasing complexity: at $Re = 50$ and 80, shed vortices remain centerline-aligned, while at $Re = 100$ and 120, vortex centers deviate and develop strong mutual interactions beyond $x = 20D$. Blockage effects further modify wake behavior: increasing confinement ratio β_s enhances vortex-boundary layer interactions that disrupt wake coherence. The extreme case $\beta_s = 0.5$ shows complete flow modification with vortices persisting only to $x \approx 5D$, contrasting with extended coherence ($x \approx 35D$) at $\beta_s = 0.2$. The Strouhal number ($St = f_s D/u_0$), representing dimensionless shedding frequency, exhibits dual dependence on both Re and β_s (Fig. 5). Confinement significantly enhances St compared to unconfined cases. Two trends emerge: (1) St increases gradually with Re due to strengthening inertial effects, and (2) St rises sharply with β_s due to amplified flow acceleration. While increased confinement suppresses downstream vortex development, it intensifies near-wake shear layer instability, leading to higher shedding frequencies and compressed vortex formation length. The observed behavior underscores how geometric confinement fundamentally alters the energy transfer mechanisms in the wake, compressing the vortex formation length while increasing the dominant instability frequency.

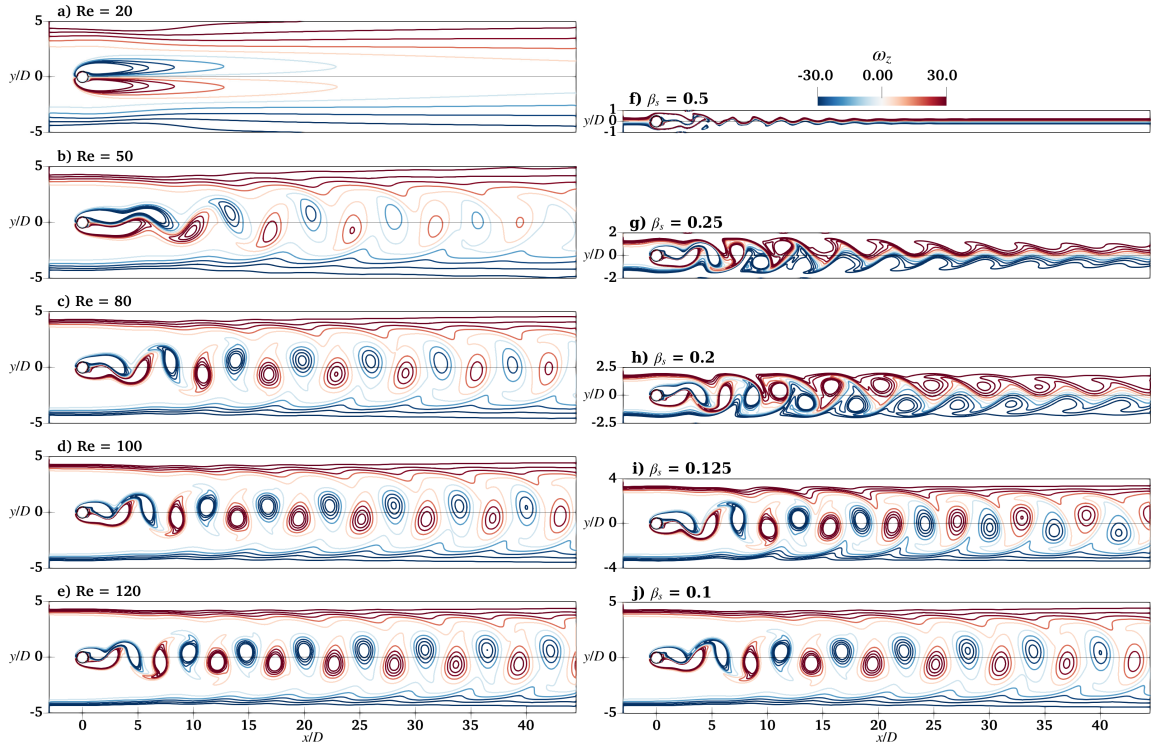
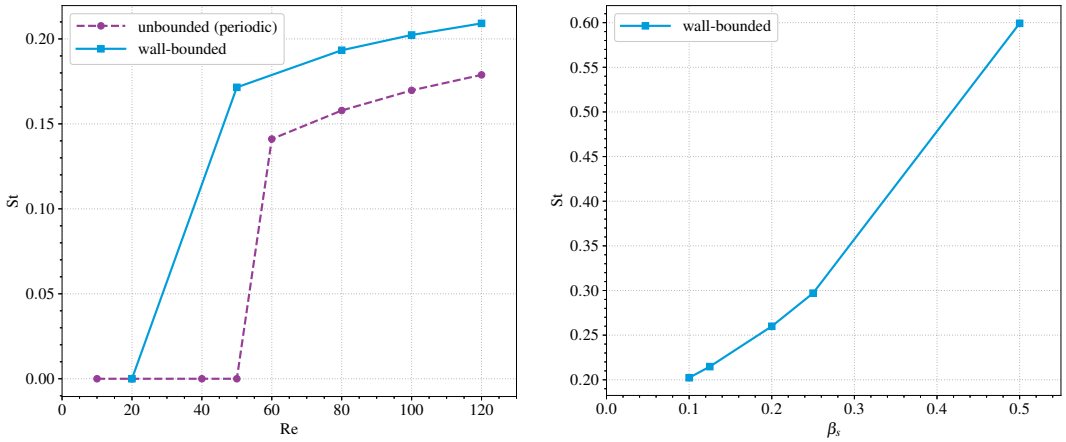


Figure 4. Comparison of instantaneous vorticity (ω_z). Left: For different Reynolds numbers, $Re = 20 - 120$. Right: For different blockage ratios, $\beta_s = 0.1 - 0.5$

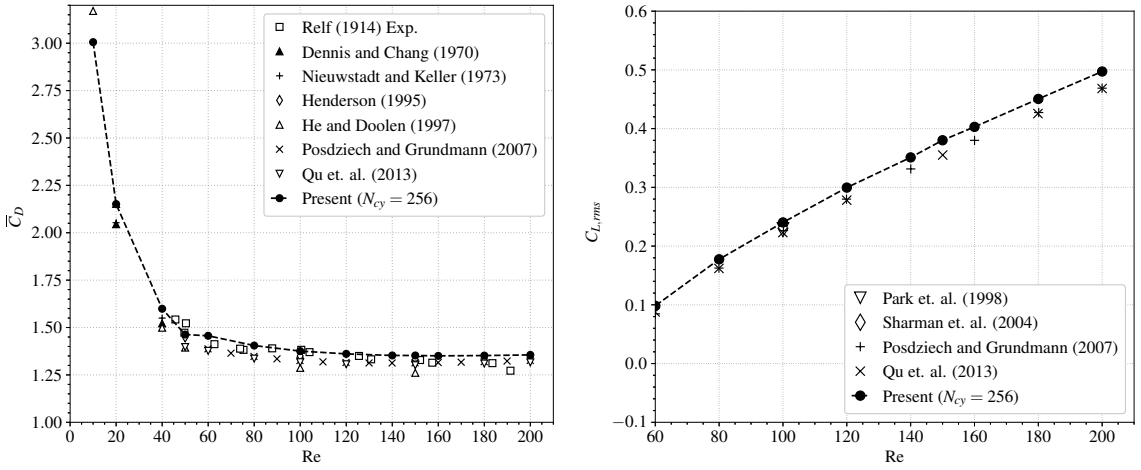


(a) (b)

Figure 5. Variation of Strouhal number (St): a) for different Reynolds numbers at a fixed blockage ratio $\beta_s = 0.1$. b) for different blockage ratio (β_s) at a fixed $Re = 100$.

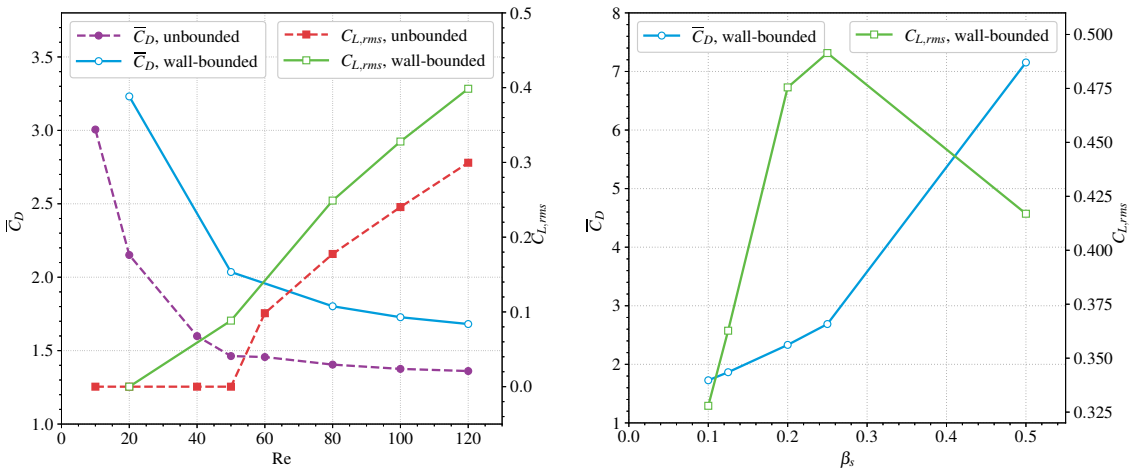
3.3 Time-averaged drag and lift coefficient analysis

The alternating vortex shedding induces time-periodic lift and drag forces on the cylinder due to asymmetric pressure distribution and wake dynamics. The time-averaged drag coefficient ($\overline{C}_D$) is then evaluated by integrating these instantaneous fluctuations, $C_d(t) = F_x(t)/(\frac{1}{2}\rho_\infty u_o^2 D)$ over several shedding cycle. Similarly, the time-averaged root-mean-square (r.m.s.) lift coefficient is calculated by integrating the instantaneous fluctuations $C'_L(t) = C_l(t) - \overline{C}_L$, where $C_l(t) = F_y(t)/(\frac{1}{2}\rho_\infty u_o^2 D)$ is the instantaneous lift coefficient and $\overline{C}_L$ is the average lift coefficient. For the unbounded (periodic) configuration, our results show good agreement with established literature data. The $\overline{C}_D$ values follow the characteristic decay with increasing Re, while $C_{L,\text{rms}}$ exhibits the expected monotonic increase, both consistent with previous numerical and experimental studies of unconfined cylinder



(a) (b)

Figure 6. Comparison results from unbounded (periodic) configuration: a) Time-averaged drag coefficient ($\overline{C}_D$); b) r.m.s. lift coefficient ($C_{L,\mathrm{rms}}$).



(a) (b)

Figure 7. Comparison of $\overline{C}_D$ and $C_{L,\mathrm{rms}}$: a) for different Reynolds numbers at a fixed blockage ratio $\beta_s = 0.1$. b) for different blockage ratio (β_s) at a fixed $Re = 100$.

flow (Fig. 6). Figures 7a and 7b present variations of $\overline{C}_D$ and $C_{L,\mathrm{rms}}$ with Reynolds number and blockage ratio, respectively. Comparisons between confined and periodic boundary conditions reveal significantly higher $\overline{C}_D$ values in wall-bounded cases, attributable to enhanced pressure drag from boundary layer development. While the Re-dependence trend remains qualitatively similar between both configurations, the confined flow demonstrates pronounced sensitivity to β_s: $\overline{C}_D$ increases non-linearly with blockage ratio due to (1) accelerated flow between the cylinder and walls, and (2) strengthened vorticity generation in the boundary layers. The $C_{L,\mathrm{rms}}$ increases monotonically with Re, attaining higher values in wall-bounded configurations compared to unconfined cases due to enhanced asymmetry in vortex shedding. However, it exhibits non-monotonic behavior with β_s, initially growing up to $\beta_s = 0.25$ followed by drastic reduction at $\beta_s = 0.5$, reflecting suppression due to strong boundary layer interactions and dampened vortex shedding.

Having established the physical accuracy of the proposed MRLBM, we now quantify its computational performance. The GPU implementation achieves a remarkable speedup of approximately 288× compared to the CPU-based counterpart, completing the simulation in only 17.89 seconds versus 5144.85 seconds for the same problem size. This corresponds to a performance of 1300 MLUPS (Million Lattice Updates Per Second) on the GPU, compared to 1.2 MLUPS on the CPU.

4 Conclusions

This study presents a GPU-accelerated MRLBM framework for simulating confined cylinder flows. Analysis of Reynolds number (Re) and blockage ratio (β_s) effects reveals three confinement mechanisms: (1) flow acceleration intensifies shear layer instabilities, elevating Strouhal numbers; (2) sharpened adverse pressure gradients increase form drag; and (3) vortex development transitions to suppressed, chaotic structures beyond $\beta_s > 0.25$. Geometric confinement dominates over inertial effects at $\beta_s \geq 0.3$, with implications for heat exchangers and offshore structures.The developed CUDA-MRLBM framework proves particularly effective for capturing these complex confinement effects across multiple flow regimes. The various parameters and coefficients obtained in this study, while specific to a blockage ratio of 0.1, provide valuable reference data for confined cylinder flows where literature data remains limited. Future studies could build upon this work by exploring wider ranges of confinement ratios and Reynolds numbers to develop more comprehensive correlations for wall-bounded flow configurations.

Acknowledgements. This work was supported by the project "Experiment-based physical and numerical modeling of subsea oil jet dispersion" under the cooperation agreement [number 0050.0125248.23.9] between UDESC and PETROBRAS. This project is governed by the investment clauses in P, D&I of the Brazilian National Agency of Petroleum, Natural Gas and Biofuels (ANP) (Resolution ANP 918/2023). The first author gratefully acknowledges the post-doctoral scholarship granted by the Graduate Program in Mechanical Engineering (PPGEM) of the Technological Sciences Center (CCT), Joinville, Santa Catarina. Finally, the authors are grateful to the anonymous referees for their valuable comments and suggestions, which significantly improved the quality of this paper.

Authorship statement. The authors hereby confirm that they are the sole liable persons responsible for the authorship of this work, and that all material that has been herein included as part of the present paper is either the property (and authorship) of the authors, or has the permission of the owners to be included here.

References

[1] K. Suzuki, T. Inamuro, A. Nakamura, F. Horai, K.-L. . Pan, and M. Yoshino. Simple extended lattice Boltzmann methods for incompressible viscous single-phase and two-phase fluid flows. *Physics of Fluids*, vol. 33, n. 3, pp. 037118, 2021.

[2] R. Zhang, X. Shan, and H. Chen. Efficient kinetic method for fluid simulation beyond the Navier-Stokes equation. *Phys. Rev. E*, vol. 74, pp. 046703, 2006.

[3] K. K. Mattila, P. C. Philippi, and J. Luiz A.. Hegele. High-order regularization in lattice-Boltzmann equations. *Physics of Fluids*, vol. 29, n. 4, pp. 046103, 2017.

[4] Hegele, L. A. and Scagliarini, A. and Sbragaglia, M. and Mattila, K. K. and Philippi, P. C. and Puleri, D. F. and Gounley, J. and Randles, A. High-Reynolds-number turbulent cavity flow using the lattice Boltzmann method. *Phys. Rev. E*, vol. 98, pp. 043302, 2018.

[5] M. Vardhan, J. Gounley, L. Hegele, E. W. Draeger, and A. Randles. Moment representation in the lattice Boltzmann method on massively parallel hardware. In *Proceedings of the International Conference for High Performance Computing, Networking, Storage and Analysis*, SC '19, New York, NY, USA. Association for Computing Machinery, 2019.

[6] X. He and L.-S. Luo. Theory of the lattice Boltzmann method: From the Boltzmann equation to the lattice Boltzmann equation. *Physical Review E*, vol. 56, n. 6, pp. 6811–6817, 1997.

[7] Ferrari, Marco A. and de Oliveira Jr., Waine B. and Lugarini, Alan and Franco, Admilson T. and Hegele Jr., Luiz A. A graphic processing unit implementation for the moment representation of the lattice Boltzmann method. *International Journal for Numerical Methods in Fluids*, vol. 95, n. 7, pp. 1076–1089, 2023.

[8] M. A. Ferrari, A. T. Franco, and J. L. A.. Hegele. Turbulent flow inside a cubic lid-driven cavity using moment representation lattice boltzmann method. *Physics of Fluids*, vol. 36, n. 7, pp. 075104, 2024.

[9] O. R. Mohammadipour, S. Succi, and H. Niazmand. General curved boundary treatment for two- and three-dimensional stationary and moving walls in flow and nonflow lattice Boltzmann simulations. *Phys. Rev. E*, vol. 98, pp. 023304, 2018.

[10] B. Sharman, F. S. Lien, L. Davidson, and C. Norberg. Numerical predictions of low Reynolds number flows over two tandem circular cylinders. *International Journal for Numerical Methods in Fluids*, vol. 47, n. 5, pp. 423–447, 2005.

[11] J.-Y. Hwang and K.-S. Yang. Drag reduction on a circular cylinder using dual detached splitter plates. *Journal of Wind Engineering and Industrial Aerodynamics*, vol. 95, n. 7, pp. 551–564, 2007.